Laser Photonics Rev., 1–10 (2011) / **DOI** 10.1002/lpor.201100003

LASER & PHOTONICS
REVIEWS

Abstract The paper reviews progress and future prospects of two kinds of planar waveguide devices; they are (a) silica and silicon photonics multi/demultiplexers for communications and signal-processing applications, and (b) a novel waveguide spectrometer based on Fourier transform spectroscopy for sensing applications.

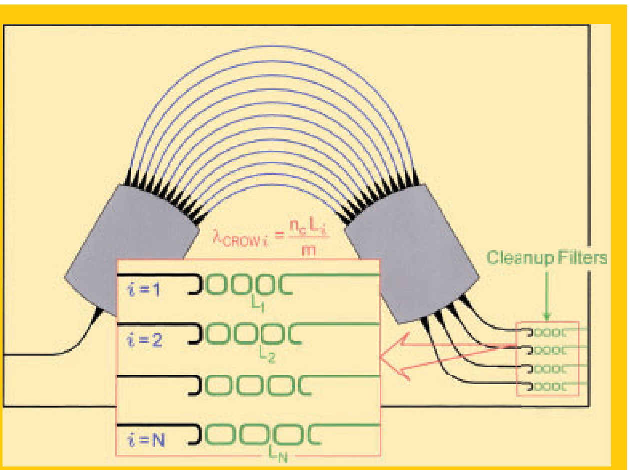

Progress and technical challenge for planar waveguide devices: silica and silicon waveguides

Katsunari Okamoto[*]

1. Introduction

Silica-based planar lightwave circuits (PLCs) are waveguide devices that integrate fiber-matched optical waveguides on silicon or glass substrate to provide an efficient means of interaction for the guided-wave optical signals. Silica PLCs are widely utilized in the current wavelength-division multiplexing (WDM), time-division multiplexing (TDM) systems and fiber-to-the-home (FTTH) access networks. The most prominent feature of the silica PLCs is their well-controlled waveguide core geometries. This allows us to fabricate multibeam or multistage interference devices such as arrayed-waveguide gratings (AWGs) and lattice-form filters [1, 2].

On the one hand, silicon photonics is widely regarded as a promising future technology to meet the requirements of rapid bandwidth growth and energy-efficient on-chip communication, while reducing cost per bit. In all potential application areas it is widely recognized that use of WDM techniques will be critical in achieving the required high levels of data transmission. Si photonics devices will have to deal with several tens of different wavelengths of light in the next-generation multicore CMOS chips and telecom and datacom applications.

There are mainly four kinds of devices capable of multi/demultiplexing tens of WDM signals; they are ring resonators, lattice-form filters, AWGs and planar Echelle gratings. The former two are cascaded devices relying on temporal multibeam interference effect and the latter two utilize spatial multibeam interference effect. In order to achieve good crosstalk characteristics in the temporal and spatial multibeam interference effects, uniformity of effective index $n_c (= \beta/k)$, where β and k denote propagation constant and wave number, is critically important. Filter characteristics of four kinds of devices will be investigated and performance limitations of silicon photonics filters are discussed.

In the latter part of the paper, an integrated-optic spectrometer based on Fourier-transform spectroscopy will be described. A novel planar waveguide spectrometer consists of interleaved Mach-Zehnder interferometer (MZI) array. The practical importance of Fourier-transform spectrometers is the ability to correct for interferometer defects caused by effective index fluctuations (phase errors) in the data-processing stage. Successful measurement results of the signal spectrum with 20-GHz resolution by the spectrometer implemented in silica-based planar waveguides will be presented.

2. Silicon-photonics WDM filters

Flat-top passband characteristics are required for filters in most of the WDM applications [1–4]. Crosstalk degradation in coupled ring resonators and lattice-form filters are caused by both gap-width error in directional couplers and optical path-length error in the waveguides.

The effective-index fluctuation δn_c in silica PLCs have been measured to be about $\delta n_c \sim 1 \times 10^{-6}$ by using Fourier transform spectroscopy [5]. Good crosstalk characteristics

---

AiDi Corporation, Tsukuba, Ibaraki 305-0032, Japan
[*] e-mail: katsu@okamoto-lab.com

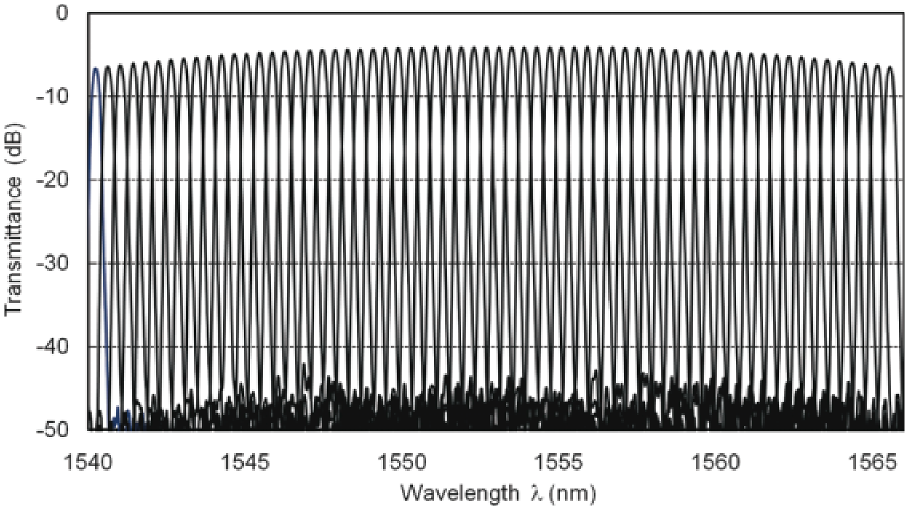

Figure 1 (online color at: www.lpr-journal.org) Demultiplexing properties of 64 ch–50 GHz spacing silica AWG.

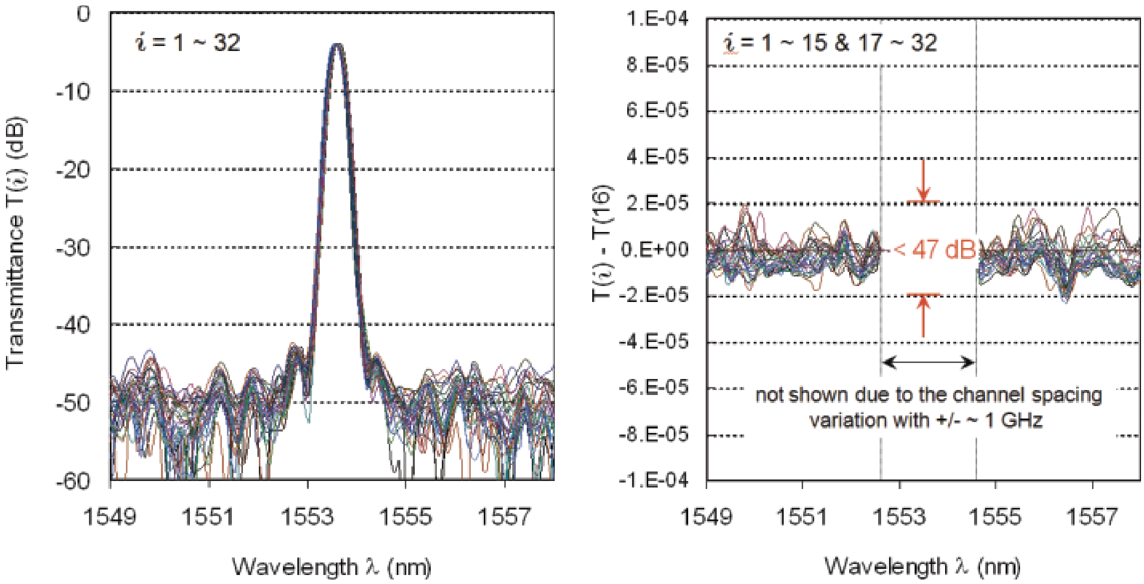

Figure 2 (online color at: www.lpr-journal.org) (a) Overlapped spectra obtained by shifting by a multiple of channel spacing and normalizing loss. (b) Difference of the transmittance $T(\mathbf{i})$ from $T(16)$.

are obtained in silica-based AWGs as shown in Fig. 1. The relation between the effective-index fluctuation δn_c and crosstalk (XT) has been investigated theoretically and experimentally [6]. Based on the investigations, the empirical expression for the relation between δn_c and XT has been obtained as

$$\mathrm{XT} \sim 10\,\mathrm{Log}\left(\frac{\delta n_c L_{\mathrm{ctr}}}{\lambda_0}\right)^2, \qquad (1)$$

where L_{ctr} and λ_0 denote array waveguide length in the middle waveguide of the array and the center wavelength of WDM signal, respectively. The waveguide length of the n-th $(n = 1 - N)$ array is expressed as $L_n = L_{\mathrm{ctr}} + (N/2 - n)\Delta L$, where ΔL is a path-length difference in the array waveguide. Then, L_{ctr} also denotes the average of the array waveguide length. L_{ctr} of AWG in Fig. 1 is $L_{\mathrm{ctr}} \sim 15$ mm. Substituting $\delta n_c \sim 1 \times 10^{-6}$, $L_{\mathrm{ctr}} \sim 15$ mm, and $\lambda_0 = 1.55\,\mu$m into Eq. (1) , we obtain XT ~ -40 dB. Although Eq. (1) gives good agreement with the experimental results, the author believes that it should be proved analytically.

Figure 2a shows the reproducibility of the spectral response of the various channels in 32 ch-50 GHz silica AWG. Similarities and differences are demonstrated by overlapping the channel spectra by shifting them by multiples of 50 GHz. The spectral shapes of the different channels overlap very well, including the side-lobe structure. In order to clearly emphasize the minute differences in the side-lobe structures, the transmittance at the central channel T(16) was subtracted from every other output $T(\mathbf{i})$ ($\mathbf{i}$ = 1–15 and 17–32) and shown in Fig. 2b. The remaining noisy features should be attributed to the effective-index fluctuations (due to the thickness variation) in the second slab region because the difference in the light path only exists in the second slab region from array waveguides to different output port. It is known from Figs. 2a and b that contribution of the effective-index fluctuation due to the thickness variation in the slab region δn_s is less than about -47 dB and can be neglected for the crosstalk degradation in the silica-based AWGs.

Based on the similar investigations on spatial multibeam interference effects in planar Echelle gratings, crosstalk can be expressed as

$$\mathrm{XT} \sim 10\,\mathrm{Log}\left(\frac{n_s 2\delta\zeta}{\lambda_0}\right)^2, \qquad (2)$$

where n_s and $\delta\zeta$ denote the effective index in the slab region and the facet position fluctuation in the reflection mirrors. It is known from Eq. (2) that $\delta\zeta$ should be about 10 nm in order to obtain -35 dB crosstalk in a silica Echelle grating ($n_s \sim 1.45$). Such a small $\delta\zeta$ would be possible in the laboratory experiments [7]. However, the mask resolution in the commercial PLC products is normally about 25–50 nm. Then, achievable crosstalk level becomes about -25 dB to -20 dB. This is why commercial planar Echelle gratings could not achieve sufficient crosstalk value to be used in the current WDM systems.

Sidewall roughness or core thickness variation may be regarded as exhibiting a zero mean value. Practically, this is not true and the mean value of the roughness normally becomes nonzero. The nonzero value in the core width or thickness variation causes effective-index fluctuation δn_c. In the spatial multibeam interference devices, such as AWGs and planar Echelle gratings, δn_c (mean value in the nth light path) also fluctuates from array waveguide to waveguide (reflection facet to facet in Echelle grating) and thus brings XT degradation. In the temporal multibeam interference devices, such as ring resonators and lattice-form filters, fluctuation of the mean value δn_c from ring to ring or MZI to MZI causes XT degradation.

Effective-index fluctuation δn_c in Si-wire waveguides has been evaluated from the measurements on the variation of resonant wavelengths in the cascaded ring resonators [8] and ring-resonator filterbanks [9]. Typical crosstalk in the drop ports was about -10dB in [9]. Channel frequencies of the filterbanks before any trimming showed large misalignment (76–467 GHz) from the target ITU frequencies. Resonance-frequency variation is evaluated to be $\delta f \sim \pm 150$ GHz ($\delta\lambda \sim \pm 1.2$ nm). It is quite large when compared with the channel frequency accuracy of $\delta f \sim \pm 2.5$ GHz ($\delta\lambda \sim \pm 0.02$ nm) in the silica AWGs [10].

After applying thermal tuning to every ring resonator, good alignment to the ITU frequency and improved crosstalk of less than -35 dB have been obtained. Average heater power for thermal tuning is about 16 mW/channel. This thermo-optic tuning power is one order of magnitude larger than the switching power in a Si-wire Mach-Zehnder switch [11]. One of the biggest advantages in silicon photonics is the ability to make energy-efficient devices. Ten times more trimming power than the switching power would not be acceptable. Therefore, we should investigate the origin of the performance degradation in silicon-photonics devices.

There are two possible origins for the performance degradation in Si-wire ring resonators; they are gap-width error in directional couplers and effective-index fluctuation δn_c in Si-wire waveguides. However, effective-index fluctuation should be the dominant factor because both channel-frequency allocation and crosstalk were improved by the thermal tuning of δn_c in the ring waveguides.

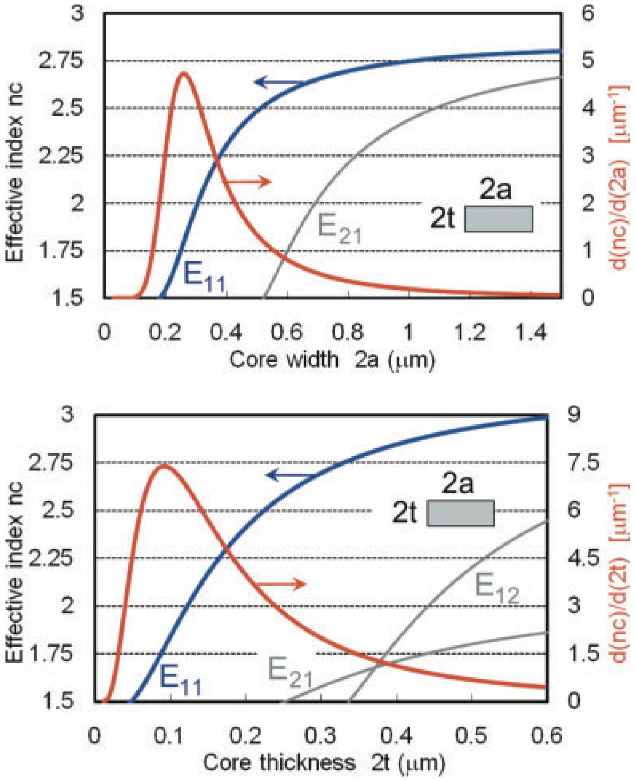

Figure 3 (online color at: www.lpr-journal.org) (a) Effective index n_c of Si-wire waveguide with 0.22 μm thickness (blue) and its dependence on the core width $2a$ (red). (b) Effective index n_c of Si-wire waveguide with 0.5 μm width (blue) and its dependence on the core width $2t$ (red).

Reported peak-to-peak resonance wavelength variations in [8] and [9] are $2\delta\lambda \sim 2.4$ nm. Then, δn_c is calculated to be $\delta n_c = n_c \delta\lambda/\lambda_0 = 1.5 - 2 \times 10^{-3}$, where $\delta n_c = 2.52$ [8], $n_c = 1.96$ [9], and $\lambda_0 = 1.55$ μm, respectively. The effective-index fluctuation δn_c in Si-wire waveguides can also be calculated by the vectorial finite element method [1]. Figure 3a shows n_c of Si-wire waveguide with thickness $2t = 0.22$ μm (blue) and its dependence on the core width $2a$ (red). $\mathrm{d}n_c/\mathrm{d}(2a)$ at the typical core width $2a = 0.5$ μm is $1.3\,\mu\mathrm{m}^{-1} = 1.3 \times 10^{-3}\,\mathrm{nm}^{-1}$. Figure 3b shows n_c of Si-wire waveguide with width $2a = 0.5$ μm (blue) and its dependence on the core thickness $2t$ (red). $\mathrm{d}n_c/\mathrm{d}(2t)$ at the typical core thickness $2t = 0.22$ μm is $3.4\,\mu\mathrm{m}^{-1} = 3.4 \times 10^{-3}\,\mathrm{nm}^{-1}$.

The core side-wall roughness of Si-wire waveguide is measured to be about $\sigma_{\mathrm{width}} \sim 2$ nm [12]. The top silicon thickness uniformity of 6-inch SOI (silicon on insulator) wafer is measured to be about ±2 nm [13]. However, the photonic device occupies just ∼1 mm square or less. Then, the thickness fluctuation would be less than $\sigma_{\mathrm{thickness}} \sim 1$ nm, as shown in the central region of Fig. 4 [14]. The effective-

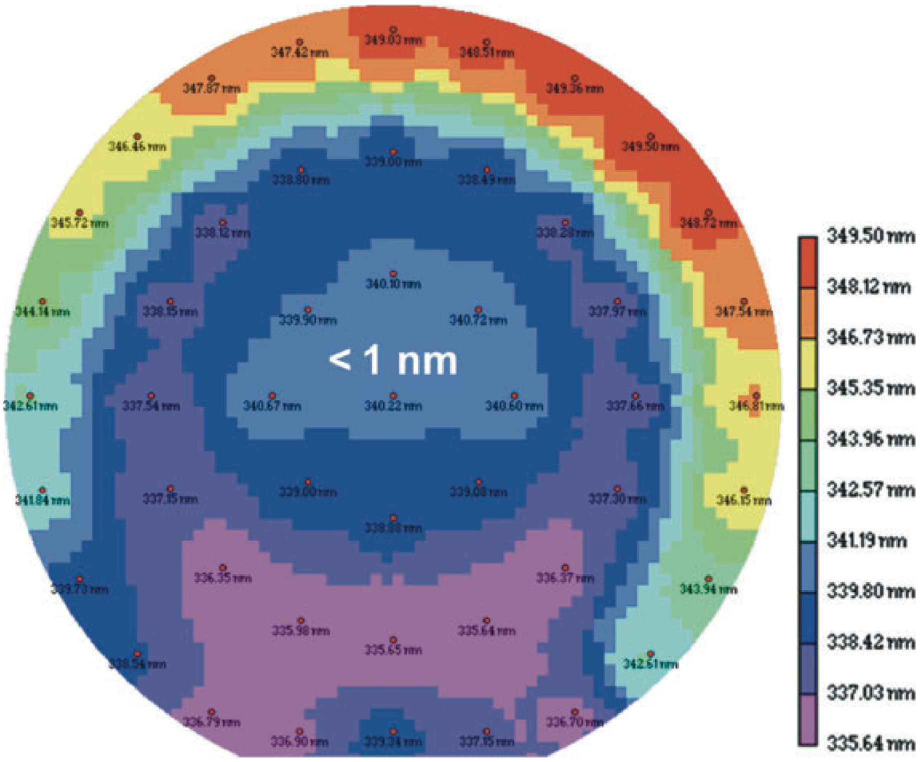

Figure 4 (online color at: www.lpr-journal.org) Thickness variation in 6-inch SOI wafer.

index fluctuation δn_c in Si-wire waveguide is then estimated to be $\delta n_c = [dn_c/d(2a)] \times \sigma_{\text{width}} \sim 2.6 \times 10^{-3}$, or $\delta n_c = [dn_c/d(2t)] \times \sigma_{\text{thickness}} \sim 3.4 \times 10^{-3}$, respectively. Both of the theoretical estimations for the effective-index fluctuation δn_c agree well with the measured value. Effective-index fluctuation δn_c against core-width variation can be reduced by enlarging core width in the straight regions. For example, $dn_c/d(2a)$ becomes $0.35\,\mu\text{m}^{-1} = 3.5 \times 10^{-4}\,\text{nm}^{-1}$ at $2a = 0.8\,\mu\text{m}$ [15] as shown in Fig. 3a.

A Si-rib waveguide structure allows us to obtain much smaller δn_c as shown in Fig. 5, where core width W, core height H, and etch depth h are $W = 0.5\,\mu\text{m}$, $H = 0.3\,\mu\text{m}$, and $h = 0.15\,\mu\text{m}$, respectively. dn_c/dW at $W = 0.5\,\mu\text{m}$ is $6.4 \times 10^{-4}\,\text{nm}^{-1}$. However, the minimum bending radius becomes much larger compared to Si-wire waveguides and makes the device size larger. Therefore, a Si-wire waveguide is still very attractive in making compact photonic devices.

Effective-index fluctuations of the order of $\delta n_c = 3 \times 10^{-4} - 2 \times 10^{-3}$determine the crosstalk values of the current Si-wire AWGs to be about −20 dB [15–17], where the typical AWG size is $L_{\text{ctr}} = 200\text{–}500\,\mu\text{m}$.

Echelle gratings have been believed to be advantageous over AWG because only the facet position error causes crosstalk degradation. But, this is not true in a Si Echelle grating since the effective-index fluctuation δn_s in the slab waveguide is substantially larger, as shown in Fig. 6. $dn_s/d(2t)$ at the typical core thickness $2t = 0.22\,\mu\text{m}$ is $3.3 \times 10^{-3}\,\text{nm}^{-1}$. Then, Eq. (2) for a Si Echelle grating

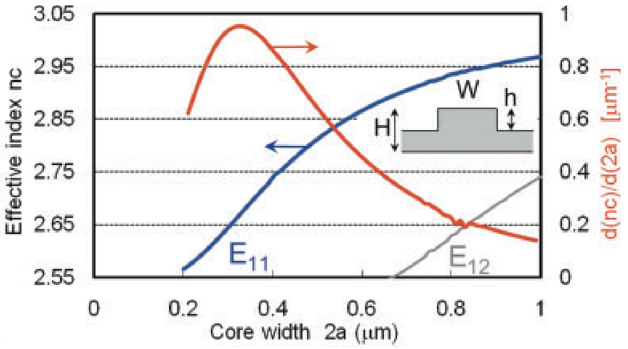

Figure 5 (online color at: www.lpr-journal.org) Effective index n_c of Si-rib waveguide (blue) and its dependence on the core width W (red).

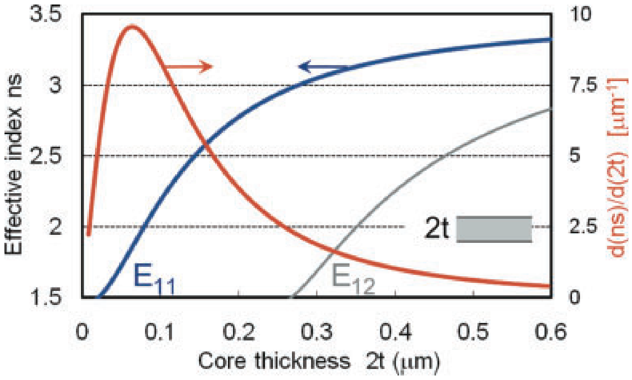

Figure 6 (online color at: www.lpr-journal.org) Effective index n_s of Si slab waveguide (blue) and its dependence on the core width 2t (red).

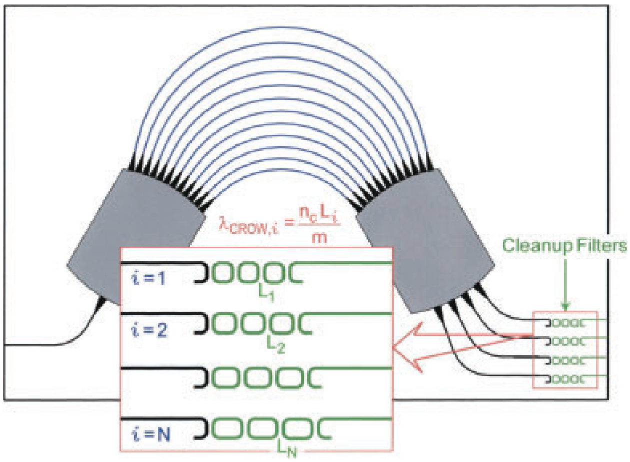

Figure 7 (online color at: www.lpr-journal.org) AWG having cleanup coupled resonator optical waveguide (CROW) filters.

should be rewritten as

$$\mathrm{XT} \sim 10\,\mathrm{Log}\left(\left|\frac{n_s 2\delta\zeta}{\lambda_0}\right| + \left|\frac{\delta n_s L_{\mathrm{ctr}}}{\lambda_0}\right|\right)^2, \qquad (3)$$

where L_{ctr} denotes the total path length in the central region of the slab. Equation (3) explains why large channel count (30 ch-3.2 nm spacing with $L_{\mathrm{ctr}} \sim 1600\,\mu\mathrm{m}$) Echelle grating has about -15 dB crosstalk, though small channel count (4 ch-20 nm spacing with $L_{\mathrm{ctr}} \sim 300\,\mu\mathrm{m}$) one had about -30 dB crosstalk [18, 19]. The total path length L_{ctr} in the large-channel count Echelle grating is almost 5 times longer than that of small channel-count one. Therefore, the second term in Eq. (3) becomes dominant in the large channel-count Echelle grating. Thickness fluctuation in SOI wafer of the order of 0.5 nm ∼ 1 nm limits the crosstalk of AWGs and Echelle gratings to about the -20 dB level.

If the thickness fluctuation in an SOI wafer could not be improved by a factor of ten, we should rely on the trimming technique such as permanent photoinduced refractive-index change [20, 21] or some novel device configuration. The author proposes an AWG (or Echelle grating) having cleanup filters at every output port, as shown in Fig. 7. Crosstalk can be largely improved without deteriorating insertion loss and bandwidth characteristics [22]. A coupled resonator optical waveguide (CROW) will be suitable for the cleanup filter because it has a large passband width.

A lattice-form filter is also attractive candidate for WDM filter applications in Si photonics. Figure 8 shows a schematic configuration of a three-stage lattice-form filter [2]. c_1 to c_4 are power coupling coefficients in the directional couplers. The channel spacing between the two output ports is given by

$$S_{\mathrm{ch}} = \frac{c}{2N_c \Delta L}, \qquad (4)$$

where ΔL, N_c, and c are path-length difference, group index ($N_c = n_c - \lambda\, dn_c/d\lambda$) of the waveguide and light velocity. In the typical Si-wire waveguide, $\Delta L = 93\,\mu\mathrm{m}$ gives the channel spacing $S_{\mathrm{ch}} = 400$ GHz. Figure 9 shows a simulated filter response without effective index fluctuation (dotted lines) and with random index fluctuation $|\delta n_c| < 5 \times 10^{-4}$ (solid lines). The effective index fluctuations in Fig. 9 were calculated by assuming $\delta n_c(\text{1st MZI}) = -4.5 \times 10^{-4}$, $\delta n_c(\text{2nd MZI}) = -4.5 \times 10^{-4}$, $\delta n_c(\text{3rd MZI}) = +4.5 \times 10^{-4}$ respectively. Other combinations of random effective index fluctuations were also investigated and the results were quite similar to the solid lines in Fig. 9.

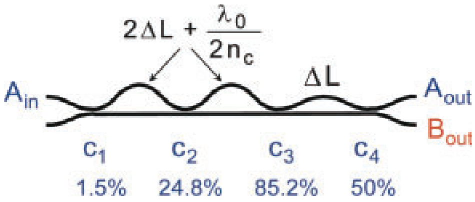

Figure 8 (online color at: www.lpr-journal.org) Three-stage lattice-form filter.

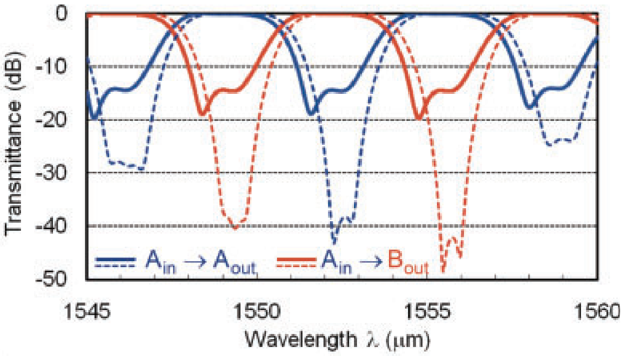

Figure 9 (online color at: www.lpr-journal.org) Filter response without effective index fluctuation (dotted lines) and random index fluctuation $|\delta n_c| < 5 \times 10^{-4}$ (solid lines).

It is shown that δn_c less than 10^{-3} degrades crosstalk characteristics drastically. Experimentally, the crosstalk level of Si-wire lattice-form filters has been limited to about -10 dB [23]. A tandem lattice-form filter configuration with employing type-I and II filters as shown in Fig. 10 [24] is quite advantageous to improve the crosstalk characteristics. The path-length difference in the type-II filter is half-λ shifted with respect to that of a type-I filter so as to adjust the filter response and thus to double the crosstalk characteristics. Dotted lines at the output port C_{out} and D_{out} are filter responses without half-λ shift and those with solid lines are responses with half-λ shift, respectively. With this elaborated configuration, chromatic dispersion caused by the filter itself can be almost completely eliminated.

Waveguide loss is another important technical challenge when discussing scaling of WDM technology. Loss in a silicon waveguide is typically ∼2 dB/cm [6], which is about 100 times larger than that of the silica waveguides (∼0.02 dB/cm [1]). On the contrary, the minimum bending radius of the silicon waveguide is ∼3 μm, which is about 1000 times smaller than that of the silica waveguides (∼3 mm). The component size of a WDM filter is not

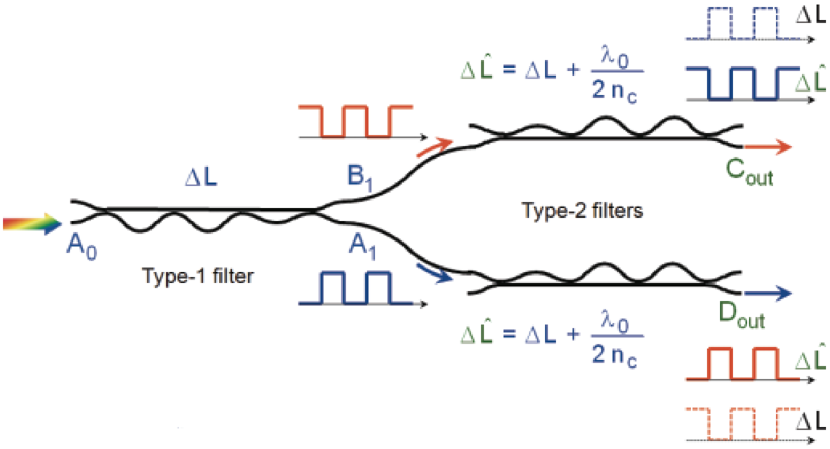

Figure 10 (online color at: www.lpr-journal.org) Tandem lattice-form filter to improve crosstalk characteristics.

normally determined by the minimum bending radius but mainly determined by the ring perimeter L_{RR} in a ring resonator and the path-length difference ΔL in a lattice-form filter, AWG, and Echelle grating. The total device size, which is represented by L_{ctr} in this article, is also proportional to the number of WDM channels N_{ch}. The typical L_{ctr} in the reported silicon photonics AWGs is $L_{\mathrm{ctr}} = 200 \sim 500\,\mu\mathrm{m}$, which is roughly 50 times smaller than that of silica PLCs. Then, insertion losses of the silicon photonics WDM filters are not so large compared to those of silica PLCs. The author believes that the waveguide loss of silicon devices would not be a critical issue.

3. Planar FT spectrometer

Spatial heterodyne spectroscopy (SHS) is an interferometric Fourier-transform technique based on a modified Michelson interferometer with no moving parts and relying on analysis of stationary interference patterns [25]. In the bulk-optic SHS, the mirrors of the Michelson interferometer are replaced by diffraction gratings to offer scanning capability for two wavefronts. The SHS concept has been generalized into a waveguide MZI array based on a cosine fast Fourier transform (FFT) [26]. The path-length difference in each asymmetrical MZI increases by ΔL, similar to AWG. For any input wavelength, the entire output of a MZI array creates spatially oscillatory patterns, where the oscillation period is wavelength dependent due to the dispersive nature of the asymmetrical MZI. Each input wavelength has a unique fringe representation, which is the basis of the Fourier-transform relation between the input spectra and the output interferogram. Employing multiple input waveguides in the waveguide SHS is an important advantage over the existing AWG-type spectrometer, since it greatly increases the light-capturing capability in proportion to the number of MZIs by using, for example, photonic lantern technology [27]. A photonic lantern is a device that efficiently converts light from a multimode fiber tip for light capturing to single-mode fibers connected to MZI input waveguides. The practical importance of the Fourier-transform spectrometer is the ability to correct for interferometer defects (phase errors) in the data-processing stage. The first waveguide SHS were fabricated in silicon-on-insulator rib waveguides using stacks of multiple MZIs [28]. However, a measurement result on the spectrum has not been reported so far to our knowledge.

The author reported a novel planar waveguide SHS configuration with an interleaved MZI array [29]. The interleaved configuration allows us to put $2 \sim 3$ times more MZIs than the simple stacking layout when we compare two layout methods for the same spectrometer parameters. We made an array of 32 MZIs in silica-based PLC. The path-length difference increment was $\Delta L = 162\,\mu\mathrm{m}$, which resulted in 20 GHz resolution in the 1.55-μm region. Phase errors in the asymmetrical MZIs were measured by the thermo-optic phase-scanning method [30]. The spectrum of the light source was successfully retrieved by correcting the MZI output data with the phase-error values.

Figure 11 shows the configuration of the novel waveguide SHS with the interleaved MZI array. The total number of MZIs is $N = 32$. The waveguide core size is $4.5\,\mu\mathrm{m} \times 4.5\,\mu\mathrm{m}$ with 1.5% refractive-index difference. The minimum bend radius is 2 mm. White boxes indicate 3-dB couplers consisting of either directional couplers or multimode interference couplers. The input and output waveguide separations at the chip ends are 15 and 50 μm, respectively. Waveguide arms in the MZI are intentionally inclined to both sides so that the waveguides intersect by more than 45^{o} with each other. It is known that the excess loss of the waveguide crossing can be reduced as low as ~ 0.02 dB/intersection when the crossing angle is larger than 45^{o} [31]. Dummy crossing waveguides are placed to make the total number of waveguide crossing equal for all MZIs. The chip size, including input and output fan-out regions, is 43 mm × 25 mm. We measured both cross-port and through-port outputs $p(k)$ and $q(k)$ in the kth ($k = 0 \sim N-1$) MZI so that the spatial nonuniformity of the input light distribution can be corrected. The output power of each port was measured by shifting the single-mode fiber in the current preliminary experiments. Fiber-to-fiber losses of MZIs are measured to be 4.2–5.4 dB.

The operational principle of a SHS spectrometer based on the MZI array has been elaborated in [26]. For a signal $s(f)$ passing through the kth MZI, a normalized cross-port

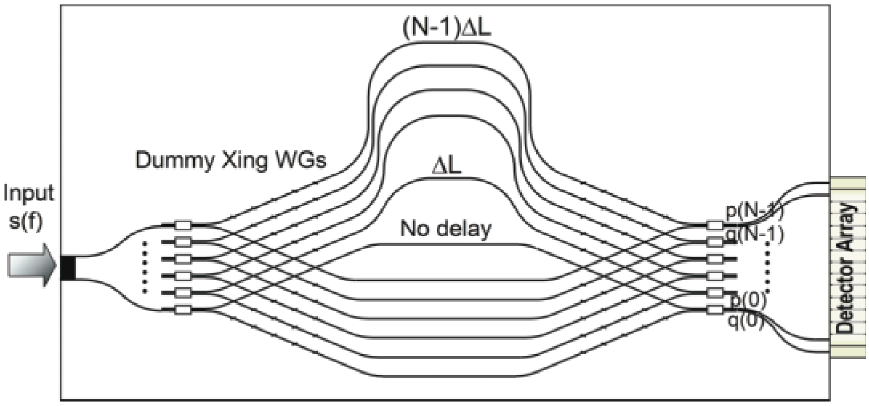

Figure 11 (online color at: www.lpr-journal.org) Planar waveguide SHS configuration with interleaved MZI array.

output is given by assuming negligible waveguide loss as

$$P(k) = \frac{p(k)}{p(k)+q(k)} = \frac{1}{S}\int_{f_0}^{f_0+\mathrm{FSR}} s(f)\frac{[1+\cos(\beta k\Delta L)]}{2}\,\mathrm{d}f \qquad (5)$$
$$(k = 0-(N-1))\,,$$

where β is a propagation constant, FSR is a free spectral range determined by ΔL, and $S = \int_{f_0}^{f_0+\mathrm{FSR}} s(f)\,\mathrm{d}f$. f_0 is denoted as the Littrow frequency at which phase delays in different MZIs become integer multiples of 2π ($\beta(f_0)\Delta L = 2m\pi$). Since the MZI response repeats periodically with FSR, one needs to block the unnecessary spectral range by a bandpass filter. Based on the discrete cosine Fourier transform, the input spectrum $s(f_n)$ ($f_n = f_0 + n\cdot\mathrm{FSR}/\hat{N}$, where $\hat{N} = 2N = 64$) can be calculated from the measured output power $P(k)$ as

$$s(f_n) = A\sum_{k=0}^{\hat{N}-1} P(k)\cos\left(2\pi\frac{nk}{\hat{N}}\right) \qquad (6)$$
$$(n = 0-(N-1))\,.$$

In the above equation, A is a constant and $P(k)$ for $k = N \sim \hat{N}-1$ is assumed to be $P(\hat{N}-k)$. Although FSR was sampled with N points in [26], we sample it with $2N$ points in order to correctly represent the MZI outputs. Because MZI responses for the signal in the upper half of FSR, $s(f_n)$ ($n = N \sim \hat{N}-1$), have identical spatial fringe representation to those of the signal in the lower half, only the lower half of the signal spectrum can be measured. Resolution of the spectrometer is given by $\delta f = c/\left(\hat{N}n_c\Delta L\right) = 20\,\mathrm{GHz}$. Phase errors caused by effective-index fluctuations in the MZI array deteriorate the accuracy in the retrieved signal by Eq. (6). The phase error $\delta\varphi_k$ in the kth MZI is expressed as $\delta\varphi_k = (2\pi/\lambda_0)\delta n_c(k)L_k$, where $\delta n_c(k)$ and L_k denote effective-index fluctuation and MZI arm length, as shown in Fig. 12a. A heater with length ℓ was placed from outside of the chip on either one of the MZI arms to measure $\delta\varphi_k$. The through-port transmittance $q(k)$ under the thermo-optic effect is given by

$$q(k) = \frac{1}{2}\left\{1-\cos\frac{2\pi}{\lambda_0}[\alpha H\ell - \delta n_c(k)L_k]\right\}. \qquad (7)$$

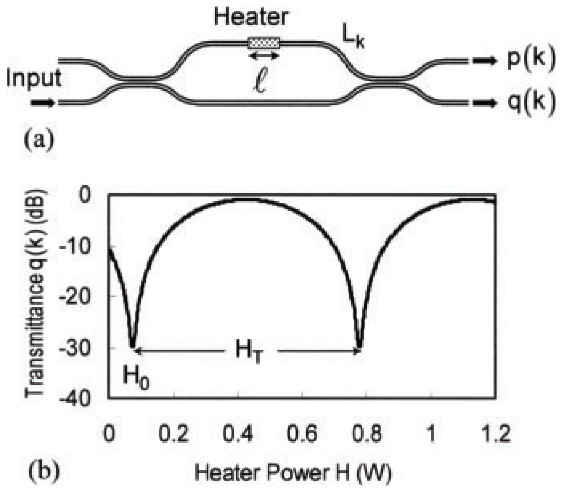

Figure 12 (a) Mach-Zehnder interferometer in the kth stage and (b) through-port response versus heater power.

Here, H is a heater power applied to the phase shifter, α is a coefficient of thermo-optic refractive-index change per unit heater power and $\lambda_0 = c/f_0$. Figure 12b shows an example of the thermo-optic phase-scanning measurement. The first extinction point indicated by H_0 corresponds to the point at which the phase error is compensated for. The power between two adjacent extinction points H_T corresponds to an optical path length change with λ_0. $\delta\varphi_k$ is then given by $\delta\varphi_k = 2\pi\cdot H_0/H_T$. The effective-index fluctuation is obtained as $\delta n_c(k) = (\delta\varphi_k/L_k)\lambda_0/2\pi$. The measured $\delta n_c(k)$ in the MZI array is shown in Fig. 13.

A major advantage of the waveguide SHS based on Fourier-transform spectroscopy is that the interferometer defects due to effective-index fluctuations can be corrected in the data-processing stage. On the contrary, physical refractive-index correction has been required for AWGs after the phase-error measurement [32]. A known signal spectrum was coupled into the waveguide SHS. The normalized cross-port output power distribution $P(k)$ and the retrieved signal spectrum $s(\lambda_n)$ ($\lambda_n = c/f_n$) by the cosine FFT are shown in Figs. 14 and 15, respectively. The Littrow wavelength λ_0 was determined by measuring the normalized cross-port output at the second MZI $P(k=1)$. $P(1)$ rapidly oscillates with respect to the wavelength

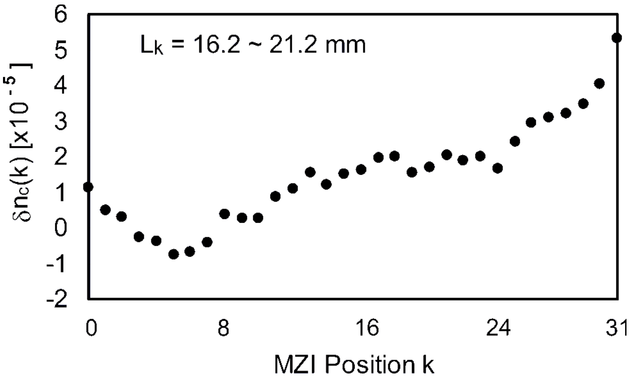

Figure 13 Measured effective-index fluctuation in the MZI array.

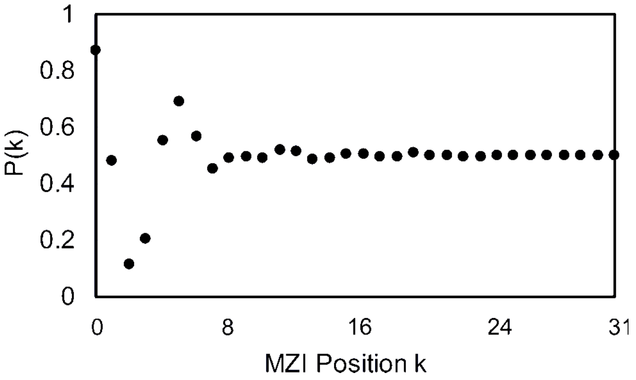

Figure 14 Measured cross-port output power distribution in the MZI array.

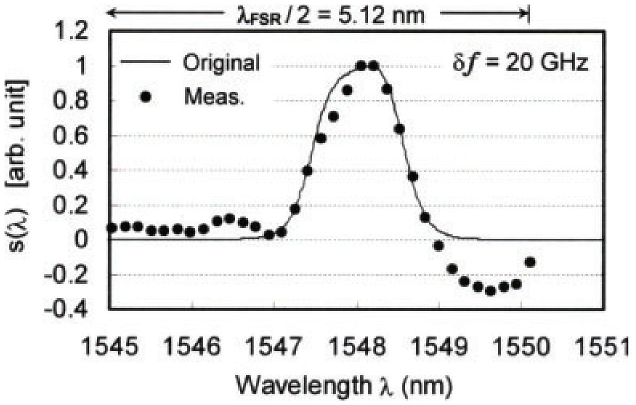

Figure 15 Retrieved signal spectrum by cosine Fourier transform.

change. But, it becomes constant and the maximum value at $\lambda_{\max} = \lambda_0[1+\delta\varphi_1/(2\pi m)] \sim \lambda_0$. λ_0 was measured to be 1550.1 nm. The solid curve in Fig. 15 is the original signal spectrum measured by a bulk spectrometer. The Hanning window was multiplied to $P(k)$ so as to reduce oscillatory features in the retrieved spectrum. The FSR in terms of wavelength is given by $\lambda_{\mathrm{FSR}} = \lambda_0/m = 10.24$ nm. Signals in the range of $\lambda = 1539.9$–1545.04 nm are not shown in Fig. 15 since they are a mirrored replica of the spectrum in $\lambda = 1545.2$–1550.1 nm. Deviation of the measured spectrum from the original one is mainly due to the phase error $\delta\varphi_k'$s since they cannot be directly included in the cosine FFT analysis. The horizontal axis in Fig. 14 is understood to be the optical path-length difference divided by $n_c\Delta L$. Then, the measured MZI output should be located at $k+\delta n_c L_k/n_c\Delta L$ instead of the ideal position, k. The correction can be done by using the measured data and the Lagrange interpolation to replace the unevenly spaced interferogram points by the evenly spaced ones [33]. Fourier-transform algorithms can then be applied to the evenly spaced interferogram points. For a large number of data points, as in bulk-optic Fourier-transform spectroscopy, a FFT-based procedure is a prerequisite. However, for a small number of N, the discretized form of Eq. (1), including phase errors,

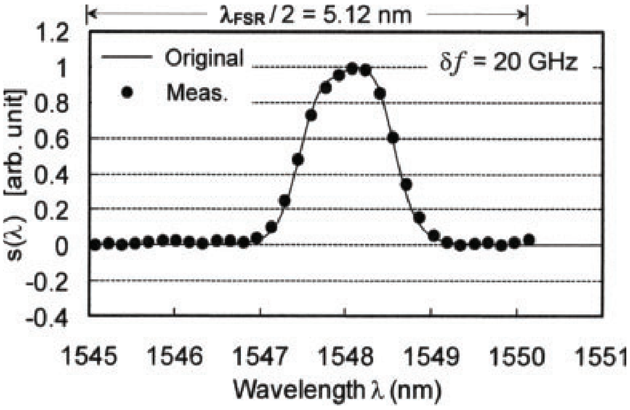

Figure 16 Signal spectrum corrected by taking account of the measured phase errors.

$$P(k) = \frac{1}{S}\sum_{n=0}^{N-1}\frac{s(f_n)}{2}\left[1+\cos\left(2\pi\frac{nk}{\hat{N}}+\delta\varphi_k\right)\right] \qquad (8)$$
$$(k = 0-(N-1)),$$

can be solved by $N\times N$ simultaneous equations. A signal spectrum corrected with the above procedure is shown in Fig. 16. The main part of the spectrum is accurately retrieved.

A phase-shift method was also proposed to generate a quadrature output from each MZI [34]. A complex Fourier transformation to a series of complex data comprising the in-phase and quadrature outputs derives the spectrum over entire FSR.

Applications of the PLC spectrometer would be varied. For medical applications, spectral measurement of oxy-hemoglobin concentration is very important to visualize metabolism of a living body. Measurement of the absorption spectra of water vapor is one of the most important issues in environmental applications. Water vapor plays a fundamental role in the dynamics and radiation budget of the atmosphere.

4. Summary

Four kinds of silicon-photonics WDM filters have been investigated in comparison with the silica-based filter devices. It is made clear that the thickness fluctuation in SOI wafer of the order of 0.5–1 nm mainly limits the crosstalk of ring resonators, lattice-form filters, AWGs and Echelle gratings to about −20 dB level. Novel AWG configuration having cleanup filters at every output port has been proposed to improve the crosstalk characteristics.

A Fourier-transform planar waveguide spectrometer has important advantages over the existing AWG-type spectrometer; they are the large optical throughput without sacrificing spectral resolution [35] and the capability of compensating phase error in the signal-processing stage. The signal spectrum was successfully retrieved by correcting the MZI output data with the phase-error values. Miniature spectrometers will be important for daily health-care and environmental-sensing applications since they are compact in size and potentially very low cost (disposable).

Received: 11 January 2011, **Revised:** 2 April 2011, **Accepted:** 28 April 2011

Key words: Silica waveguide, silicon photonics, SOI, AWG, Echelle grating, ring resonator, lattice-form filter, spectroscopy, Fourier transform.

Katsunari Okamoto received the B. S., M. S., and Ph. D. degrees in electronics engineering from Tokyo University, Tokyo, Japan, in 1972, 1974, and 1977, respectively. He joined Ibaraki Electrical Communication Laboratory, Nippon Telegraph and Telephone Corporation (NTT), Ibaraki, Japan, in 1977. From 1982 to 1983, he worked as a guest researcher at Optical Fiber Group, Southampton University, Southampton, England. From July 2006, he has worked as Professor of Electrical and Computer Engineering at the University of California at Davis (UC Davis). His research at UC Davis includes passive and active photonics devices and silicon photonics. He is currently working as CTO at AiDi corporation aiming at the miniature lightwave spectroscopic sensors for environmental sensing and health diagnostics.

References

[1] K. Okamoto, Fundamentals of Optical Waveguides, 2nd edn. (Elsevier, New York, 2006), Chap. 9.
[2] K. Jinguji and M. Oguma, IEEE J. Lightwave Technol. **18**(2), 252–259 (2000).
[3] A. Yariv, Y. Xu, R. K. Lee, and A. Scherer, Opt. Lett. **24**(11), 711–713 (1999).
[4] Z. Shi and S. He, IEEE J. Selec. Top. Quantum Electron. **8**(6), 1179–1185 (2002).
[5] K. Takada, Y. Inoue, H. Yamada, and M. Horiguchi, Electron. Lett. **30**(20), 1671–1672 (1994).
[6] K. Okamoto, in: Proceedings of the International Conference on Fiber Optics and Photonics (Photonics 2010), Guwahati, India, 2010.
[7] S. Janz, A. Balakrishnan, S. Charbonneau, P. Cheben, M. Cloutier, A. Delage, K. Dossou, L. Erickson, M. Gao, P. A. Krug, B. Lamontagne, M. Packirisamy, M. Pearson, and D. X. Xu, IEEE J. Lightwave Technol. **16**(2), 503–505 (2004).
[8] F. Xia, L. Sekaric, and Y. Vlasov, Nature Photon. **1**(1), 65–71 (2007).
[9] M. S. Dahlem, C. W. Holzwarth, A. Khilo, F. X. Kärtner, H. I. Smith, and E. P. Ippen, Opt. Express **19**(1), 306–316 (2011).
[10] Wavelength accuracy data for commercial silica AWG: http://www.ntt-electronics.com/en/products/photonics/awg_mul_d.html, 12 May 2011.
[11] S. Sekiguchi, T. Kurahashi, K. Kawaguchi, and K. Morito, Proceedings of the 23rd Annual Meeting of the IEEE Photonics Society, WW3, Denver, Colorado, 2010.
[12] M. Romagnoli, in: Proceedings of the European Conference on Optical Communication ’07 Workshop, Berlin 2007.
[13] D. Van Thourhout and W. Bogaerts, in: Proceedings of the Optical Fiber Communication Conference ’10, OtuB5, San Diego, CA, 2010.
[14] W. A. Zortman, D. C. Trotter, and M. R. Watts, Opt. Express **18**(23), 23598–23607 (2010).
[15] W. Bogaerts, P. Dumon, D. Van Thourhout, D. Taillaert, P. Jaenen, J. Wouters, S. Beckx, V. Wiaux, and R. G. Baets, IEEE J. Select. Top. Quantum Electron. **12**(6), 1394–1401 (2006).
[16] D. J. Kim, J. M. Lee, J. H. Song, J. Pyo, and G. Kim, IEEE Photon. Technol. Lett. **20**(19), 1615–1617 (2008).
[17] Q. Fang, T. Y. Liow, J. F. Song, K. W. Ang, M. B. Yu, G. Q. Lo, and D. L. Kwong, Opt. Express **18**(5), 5106–5113 (2010).
[18] J. Brouckaert, W. Bogaerts, P. Dumon, D. Van Thourhout, and R. Baets, IEEE J. Lightwave Technol. **25**, 1269–1275 (2007).
[19] W. Bogaerts, S. K. Selvaraja, P. Dumon, J. Brouckaert, K. D. Vos, D. Van Thourhout, and R. Baets, IEEE J. Select. Top. Quantum Electron. **16**(1), 33–44 (2010).
[20] A. H. Nejadmalayeri, P. R. Herman, J. Burghoff, M. Will, S. Nolte, and A. Tünnermann, Opt. Lett. **30**(9), 964–966 (2005).
[21] Y. Shen, I. B. Divliansky, D. N. Basov, and S. Mookherjea, in: Proceedings of the Optical Fiber Communication Conference ’11, PDPC3, Los Angeles, CA, 2011.
[22] S. Kamei, A. Kaneko, M. Ishii, T. Shibata, Y. Inoue, and Y. Hibino, IEEE J. Lightwave Technol. **23**(5), 1929–1938 (2005).
[23] F. Horst, W. M. J. Green, B. J. Offrein, and Y. A. Vlasov, Proc. SPIE **7386**, 73862L1–L9 (2009).
[24] M. Oguma, T. Kitoh, Y. Inoue, T. Mizuno, T. Shibata, M. Kohtoku, and Y. Hibino, IEEE J. Lightwave Technol. **22**(3), 895–902 (2004).
[25] J. M. Harlander, F. L. Roesler, J. G. Cardon, C. R. Englert, and R. R. Conway, Appl. Opt. **41**(7), 13431352 (2002).
[26] M. Florjańczyk, P. Cheben, S. Janz, A. Scott, B. Solheim, and D. X. Xu, Opt. Express **15**(26), 18176–18189 (2007).
[27] D. Noordegraaf, P. M. W. Skovgaard, M. D. Maack, J. B. Hawthorn, R. Haynes, and J. Lagsgaad, Opt. Express **18**(5), 4673–4678 (2010).

[28] M. Florjańczyk, P. Cheben, S. Janz, B. Lamontagne, J. Lapointe, A. Scott, B. Solheim, and D. X. Xu, Proc. SPIE **7394**, 75940R1–R9 (2010).

[29] K. Okamoto, H. Aoyagi, and K. Takada, Opt. Lett. **35**(12), 2103–2105 (2010).

[30] T. Goh, S. Suzuki, and A. Sugita, IEEE J. Lightwave Technol. **15**(11), 2107–2113 (1997).

[31] T. Kominato, T. Kitoh, K. Katoh, Y. Hibino, and M. Yasu, in: Proceedings of the OptoElectronics Conference OEC'92, Makuhari, Japan, 1992, Paper 16B4-1, pp. 138–139.

[32] K. Takada, T. Tanaka, M. Abe, T. Yanagisawa, M. Ishii, and K. Okamoto, Electron. Lett. **36**(1), 60–61 (2000).

[33] G. Fan and Q. H. Liu, IEEE Trans. Antenn. Propag. **52**(2), 461–465 (2004).

[34] K. Takada, H. Aoyagi, and K. Okamoto, Electron. Lett. **46**(24), 1620–1621 (2010).

[35] N. K. Fontaine, K. Okamoto, T. Su, and S. J. B. Yoo, in: Proceedings of the Optical Fiber Communication Conference '11, OWM2, Los Angeles, CA, 2011.